

# Smoothed particle hydrodynamics and element bending group modeling of flexible fibers interacting with viscous fluids

Xiufeng Yang,<sup>1,\*</sup> Moubin Liu,<sup>2,†</sup> and Shiliu Peng<sup>1</sup>

<sup>1</sup>*Institute of Mechanics, Chinese Academy of Sciences, Beijing 100190, China*

<sup>2</sup>*College of Engineering, Peking University, Beijing 100187, China*

(Received 27 August 2014; published 15 December 2014)

This paper presents a smoothed particle hydrodynamics (SPH) and element bending group (EBG) coupling method for modeling the interaction of flexible fibers with moving viscous fluids. SPH is a well-developed mesh-free particle method for simulating viscous fluid flows. EBG is also a particle method for modeling flexible bodies. The interaction of flexible fibers with moving viscous fluids is rendered through the interaction of EBG particles for flexible fiber and SPH particles for fluid. In numerical simulation, flexible fibers of different lengths are immersed in a moving viscous fluid driven by a body force. The drag force on the fiber obtained from SPH-EBG simulation agrees well with experimental observations. It is shown that the flexible fiber demonstrates three typical bending modes, including the U-shaped mode, the flapping mode, and the closed mode, and that the flexible fiber experiences a drag reduction due to its reconfiguration by bending. It is also found that the  $U^{4/3}$  drag scaling law for a flexible fiber is only valid for the U-shaped mode, but not valid for the flapping and closed modes. The results indicate that the reconfiguration of a flexible fiber is caused by the fluid force acting on it, while vortex shedding is of importance in the translations of bending modes.

DOI: [10.1103/PhysRevE.90.063011](https://doi.org/10.1103/PhysRevE.90.063011)

PACS number(s): 47.32.-y, 47.11.-j, 46.40.-f, 83.50.-v

## I. INTRODUCTION

An object immersed in a viscous fluid will experience a drag force due to the interaction of the body and the fluid, if the object moves through the fluid or the fluid flows around the object [1]. How to accurately predict and effectively reduce the drag is of great importance in both engineering and sciences. In general, the drag is a function of the relative velocity between the object and the fluid. For a rigid object, the drag is proportional to the square of the velocity [1]. Therefore as the speed of a moving rigid body increases, the drag force can increase significantly, which further hinders the movement of the object. The drag also depends on the shape of the object, and a streamline shape can result in small drag. This can be seen from different designs for aircraft, land, and underwater vehicles with streamline shapes. For a flexible object, the drag may increase slower than the square of velocity because of the reconfiguration of the object caused by fluid forces [2–5]. As can be observed in nature, many living organisms (e.g., trees, plants, seaweed, and coral beds) can change their shape in moving fluids to reduce drag [6–9]. On the one hand, the reconfiguration makes the frontal area presented to the flow become smaller, which can reduce the drag. On the other hand, the reconfiguration makes the shape of the object more streamlined, which can further decrease the drag.

According to many experiments on plants and considering the effect of reconfiguration, Vogel [2,6] concluded that the fluid drag on a flexible object is lower than the square of velocity, which can be described as

$$D \propto U^\beta, \quad (1)$$

where  $D$  is fluid drag,  $U$  is the velocity, and  $\beta$  represents an exponent. In general, the exponent  $\beta$  has a value around 2 for a rigid body, while it has a value smaller than 2 for a flexible object. Alben *et al.* [10,11] experimentally and theoretically studied the drag reduction for a flexible fiber immersed in a flowing soap film. Their results indicated a transition from the  $U^2$  drag scaling for rigid fibers to a  $U^{4/3}$  drag scaling for flexible fibers, which shows that the value of  $\beta$  for a flexible fiber is  $4/3$ . By dimensional asymptotic analysis, Gossellin *et al.* [12] obtained the same exponent  $\beta = 4/3$  for flexible fibers and rectangular flexible plates. They also obtained the exponent  $\beta = 1$  for flexible disks and the exponent  $\beta = 2/3$  for disks rolling up into cones in flows [12]. Considering the posture-dependent drag and the restoring force due to vegetation stiffness and buoyancy, Luhar and Nepf [13] proposed a theoretical model to predict drag and posture for plants and natural systems.

With the advancement of the computer hardware and computational technique, it would be attractive to investigate the interaction of flexible fibers with fluid flows by numerical modeling. Numerical simulation of flexible fibers interacting with fluid flows is usually a great challenge for conventional grid-based numerical methods, as the fluid-flexible fiber interaction involves moving interfaces and deformable boundaries. Due to the complexity of the problem, there is only a very limited amount of literature describing the numerical modeling of flexible fibers interacting with fluid flows. Zhu and Peskin [14] numerically studied the drag of a flexible fiber immersed in a two-dimensional (2D) incompressible flow for Reynolds number in the range of 12.5–375 using the immersed boundary (IB) method. They found that fiber mass had little effect on the drag at a certain range. Zhu [15] investigated the vortex shedding and drag coefficient of a flexible fiber for Reynolds number in the range of 30–800. However, there are plenty of experiments with flexible bodies at much higher Reynolds numbers.

The numerical difficulty in modeling fluid-flexible fiber interaction is the treatment of moving interfaces and

\*Corresponding author: yangxf@imech.ac.cn

†mbliu@pku.edu.cn

deformable boundaries. As such, a numerical approach that can well treat moving interfaces and deformable boundaries would be appealing in modeling fluid-flexible fiber interaction. In this paper, we present such a numerical approach for studying the drag reduction of flexible fiber immersed in fluid for high Reynolds numbers as well as low Reynolds numbers. The numerical approach is based on the coupling of the smoothed particle hydrodynamics (SPH) method and the element bending group (EBG) method.

SPH is a “truly” mesh-free particle method, which was first invented to solve astrophysical problems in three-dimensional open space [16,17] and later extended for many other problems [18–20]. In SPH, the state of a system is represented by a set of particles which possess material properties and interact with each other within a range controlled by a weight function or smoothing function [21,22]. As a Lagrangian particle method, SPH conserves mass exactly. In SPH, there is no explicit interface tracking for multiphase flows—the motion of the fluid is represented by the motion of particles, and fluid surfaces or fluid-fluid interfaces move with particles representing their phase defined at the initial stage. The mesh-free nature of SPH method removes the difficulties due to the large deformations, since SPH uses particles rather than mesh as a computational frame to approximate related governing equations. Therefore SPH is well suited for fluid flows with moving interfaces.

The EBG technique can also be regarded as a particle method. It was first proposed for modeling membrane structures, which can be considered as elastic shells [23], and was later extended to model red blood cell (RBC) membranes [24,25]. A flexible fiber can also be considered as a membrane structure. In the EBG model, an EBG consists of two adjacent line segments connecting three neighboring particles. Except for the tension force, the bending moment needs to be considered when modeling the movement and deformation of a flexible body. The bending moments on an EBG can be converted into pairs of forces acting on the three neighboring particles. Hence the EBG method can be attractive in modeling the movement and deformation of flexible bodies.

By coupling SPH with EBG, it is possible to model the fluid-flexible fiber interaction. SPH particles are used to model the viscous fluid flow governed by Navier-Stokes equations, and EBG particles are used to model the dynamic movement and deformation of flexible fibers. The interaction of the neighboring fluid (SPH) and fiber (EBG) particles renders the fluid-flexible fiber interaction. The idea of SPH-EBG coupling was originally proposed by Hosseini and Feng [25] to simulate RBC deformations in shear flows, and the reported numerical results demonstrated good consistence with the experimental observations.

The paper is organized as follows. In Sec. II, the physical model and methodology are described. In Sec. III, numerical results and some discussions are provided, while special interests are focused on the validation of the SPH-EBG approach together with the visualization of the vortex structure in particle methods, the morphology evolution of the flexible fiber, and the effects of flexibility on the drag. The paper ends in Sec. IV with some further remarks.

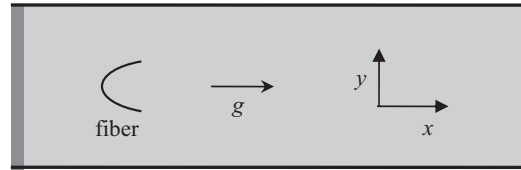


FIG. 1. A sketch of the computational settings. The midpoint of the fiber is fixed in the midline of the channel, while the two ends of the fiber are free to move. The system is initially at rest and the flow is driven by a body force  $g$  in the  $x$  direction. The periodic boundary condition is implemented in the  $x$  direction, and there is a layer of porous media at the flow inlet area.

## II. PHYSICAL MODEL AND METHODOLOGY

### A. Physical model

Figure 1 shows the computational settings for the physical model. This is a 2D flow channel with a one-dimensional (1D) fiber immersed in the flow. The midpoint of the fiber is fixed in the midline of the channel, while the two ends of the fiber are free to move. The upper and lower boundaries are solid wall. The left and right boundaries are flow inlet and outlet. The periodic boundary condition is implemented in the main flow direction ( $x$  direction). In order to remove the flow effects on inlet flow from outlet flow due to the periodical boundary condition, a layer of porous media is deployed in the left end (flow inlet) of the flume. The treatment of inlet and outlet flow condition is further discussed later. In order to study the influence of the flexibility on the drag scaling, both flexible and rigid fibers were simulated.

In order to compare with experiments, the computational settings are similar to the experimental setup used by Alben *et al.* [10] and the key physical values are the same as those in the experiment. The difference between our numerical simulation and Alben *et al.*'s experiment is that the flow in our simulation is a 2D, while the soap film used in the experiment is a quasi-2D flow.

The length and width of the channel are 0.4 and 0.09 m, respectively. The density and dynamic viscosity of the fluid are  $1000 \text{ kg/m}^3$  and  $0.004 \text{ N s/m}^2$ , respectively. It should be noted that in 2D numerical simulations the flow quantities are uniform in the out-of-plane direction. The flow thickness can be regarded as 1 m. The thickness of soap film used in the experiment [10] is within the range of 1–3  $\mu\text{m}$ . Therefore the thickness of the 2D flow is 6 orders ( $1 \text{ m}$  versus  $10^6 \mu\text{m}$ ) higher than the thickness of soap film in the experiment. The rigidity of the flexible fiber used in the 2D simulation is  $2.8 \times 10^{-3} \text{ J m}$ , which is also 6 orders higher than the rigidity of the flexible fiber used in the experiment, that is,  $2.8 \times 10^{-9} \text{ J m}$ . Three flexible fibers and a rigid fiber are used in our simulations. The lengths of the flexible fibers are 3.3, 5.0, and 8.0 cm, respectively, and the length of the rigid fiber is 2.0 cm. The density of the fiber is the same as the fluid, so the buoyancy and the gravity of the fiber can offset.

The system is initially at rest and the flow is driven by a body force  $g$  in the  $x$  direction (the flow direction). If the body force  $g$  takes the value of the gravitational acceleration (i.e.,  $9.8 \text{ m/s}^2$ ), the mean velocity of the flow will increase very rapidly at the initial stage, and then the velocity increment

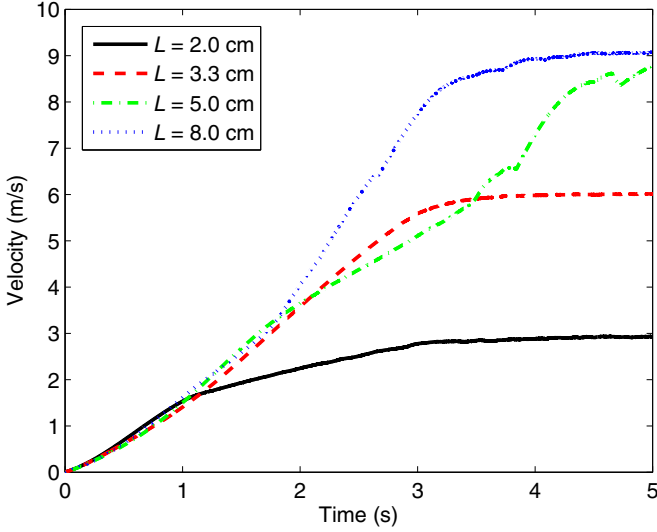


FIG. 2. (Color online) Mean flow velocity versus time for a rigid fiber of length  $L = 2.0$  cm and three flexible fibers of length  $L = 3.3, 5.0,$  and  $8.0$  cm.

will be smaller and smaller due to the growth of the drag between the fluid and the fiber. The flow velocity will approach a maximum value when the body force equals the drag on the fiber and the viscous force from the channel walls. In order to make the mean velocity of the flow increase slowly at the initial stage, the magnitude of the body force  $g$  used in our simulation varies with time  $t$  as follows:

$$g = \begin{cases} 0.8 + 3t, & t \leq 3 \\ 9.8, & t > 3 \end{cases}, \quad (2)$$

where the units of  $g$  and  $t$  are  $\text{m/s}^2$  and s, respectively. Driven by this body force, the mean velocity of the flow is shown in Fig. 2. It can be seen that the increase of each mean velocity is roughly linear before it reaches a plateau except for the fiber of length  $L = 5.0$  cm; this is mainly caused by the flapping of the fiber (see Sec. III).

### B. SPH method for viscous fluid

In this paper the fluid flow is modeled by the SPH method, which uses a set of particles to represent the state of the simulated system. The particles possess individual material properties, move according to corresponding governing conservation equations, and act as the computational frame for field variable approximations. Specifically, in the SPH method, for any function  $A(\mathbf{r})$  which is a function of the spatial position  $\mathbf{r}$ , the value of function  $A$  at a certain point  $a$  whose position vector is  $\mathbf{r}_a$  can be approximated by the following integral interpolation:

$$A(\mathbf{r}_a) = \int_{\Omega} A(\mathbf{r})W(\mathbf{r}_a - \mathbf{r}, h)dV, \quad (3)$$

where  $W(\mathbf{r}_a - \mathbf{r}, h)$  is a smoothing or kernel function;  $h$  is a smoothing length which, if multiplied by a scalar factor  $k$  which is determined by the kernel function, defines the influence domain of the smoothing function;  $dV$  is a differential volume element; and  $\Omega$  is an integral domain. The interpolation reproduces  $A$  exactly if the kernel is a  $\delta$

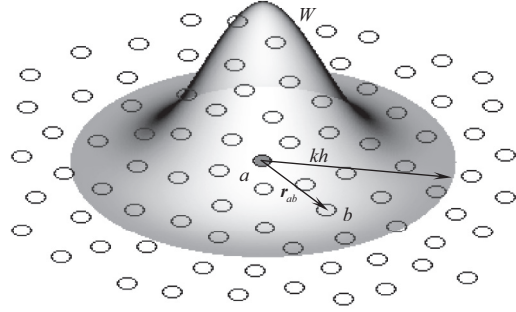


FIG. 3. Sketch of kernel interpolation of SPH particles. As the distance between two particles increases, the mutual influence between the two particles reduces.

function. In practice, the value of  $h$  determines the range of the integral domain and the kernel  $W$  tends to the  $\delta$  function as the smoothing length  $h$  tends to zero. Kernels are normalized to 1 so that constants are interpolated exactly. In our simulations, the smoothing length is equal to the initial particle spacing.

When representing a fluid domain with discrete SPH particles, the interpolation is approximated by a summation interpolation over the particles:

$$A_a = \sum_b A_b W_{ab} \frac{m_b}{\rho_b}, \quad (4)$$

where  $W_{ab} = W(\mathbf{r}_a - \mathbf{r}_b, h)$ ; the indexes  $a$  and  $b$  denote labels of particles, e.g.,  $A_a$  denotes the value of quantity  $A$  at  $\mathbf{r}_a$ , and particle  $b$  has position  $\mathbf{r}_b$ , mass  $m_b$ , density  $\rho_b$ , and volume  $m_b/\rho_b$ . The summation is over all particles, but in practice it is only over near neighbors because the kernel  $W$  vanishes outside its support domain (see Fig. 3). In this work the commonly used cubic spline kernel function is used as follows:

$$W(s, h) = \alpha_d \begin{cases} (2-s)^3 - 4(1-s)^3, & 0 \leq s < 1 \\ (2-s)^3, & 1 \leq s < 2 \\ 0, & s \geq 2 \end{cases}, \quad (5)$$

where  $s = r/h$ ,  $r$  is the distance between two particles, and  $\alpha_d$  is the normalization factor, with a value of  $1/6h$ ,  $5/(14\pi h^2)$ , and  $1/(4\pi h^3)$  in one-, two-, and three-dimensional space, respectively.

The gradient of  $A$  can be obtained by differentiating Eq. (4) as

$$\nabla A_a = \sum_b \frac{m_b}{\rho_b} A_b \nabla_a W_{ab}, \quad (6)$$

where  $\nabla_a W_{ab} = W'_{ab} \mathbf{r}_{ab}/|\mathbf{r}_{ab}|$  is the gradient of the kernel taken with respect to the position of particle  $a$ , and  $\mathbf{r}_{ab} = \mathbf{r}_a - \mathbf{r}_b$ .

It is shown in Eqs. (4) and (6) that SPH provides a numerical approach for discretizing partial differential equations (PDEs). For viscous fluid flows, the Navier-Stokes (N-S) equations are written in Lagrangian form as

$$\frac{d\rho}{dt} = -\rho \nabla \cdot \mathbf{u}, \quad (7)$$

$$\frac{d\mathbf{u}}{dt} = \mathbf{g} - \frac{1}{\rho} \nabla p + \frac{\mu}{\rho} \nabla^2 \mathbf{u}, \quad (8)$$

where  $\rho$  is fluid density,  $\mathbf{u}$  is the velocity vector,  $p$  is pressure,  $\mu$  is the dynamic viscosity, and  $\mathbf{g}$  denotes the body force including the gravitational acceleration.

Applying SPH to Eqs. (7) and (8), the Lagrangian form of the N-S equations can be written in the following discretized SPH formulations:

$$\frac{d\rho_a}{dt} = \sum_b m_b \mathbf{u}_{ab} \cdot \nabla_a W_{ab}, \quad (9)$$

$$\begin{aligned} \frac{d\mathbf{u}_a}{dt} = & \mathbf{g}_a - \sum_b m_b \left( \frac{P_a}{\rho_a^2} + \frac{P_b}{\rho_b^2} \right) \cdot \nabla_a W_{ab} \\ & + \sum_b \frac{m_b(\mu_a + \mu_b) \mathbf{r}_{ab} \cdot \nabla_a W_{ab}}{\rho_a \rho_b (r_{ab}^2 + 0.01h^2)} \mathbf{u}_{ab}, \end{aligned} \quad (10)$$

where  $\mathbf{u}_{ab} = \mathbf{u}_a - \mathbf{u}_b$ ,  $\mathbf{r}_{ab} = \mathbf{r}_a - \mathbf{r}_b$ ,  $r_{ab} = |\mathbf{r}_{ab}|$ . The term  $0.01h^2$  is added to prevent singularities of the viscous term when two particles approach each other infinitely. Details of SPH formulations for the N-S equations can be found in more SPH references [21,26].

In SPH, incompressible fluids can be treated as slight compressible fluids using an artificial equation of state. In this paper, the following equation of state [19] is used:

$$P(\rho) = c^2(\rho - \rho_0), \quad (11)$$

where  $\rho_0$  is a reference density, and  $c$  is a numerical speed of sound. In order to reduce the density fluctuation down to 1%,  $c$  is usually taken 10 times higher than the maximum fluid velocity [19].

In order to model the surface tension effect, an artificial interparticle force  $\mathbf{F}^I$  is added in the momentum equation (10) as follows:

$$\begin{aligned} \frac{d\mathbf{u}_a}{dt} = & \mathbf{g}_a - \sum_b m_b \left( \frac{P_a}{\rho_a^2} + \frac{P_b}{\rho_b^2} \right) \cdot \nabla_a W_{ab} \\ & + \sum_b \frac{m_b(\mu_a + \mu_b) \mathbf{r}_{ab} \cdot \nabla_a W_{ab}}{\rho_a \rho_b (r_{ab}^2 + 0.01h^2)} \mathbf{u}_{ab} + \sum_b \frac{\mathbf{F}_{ab}^I}{m_a}, \end{aligned} \quad (12)$$

where  $\mathbf{F}_{ab}^I$  is the artificial interparticle force acting on particle  $a$  due to particle  $b$ . The force is similar to the particle-particle interaction given by Tartakovsky and Meakin [27] when modeling surface tension and contact angles with SPH as follows:

$$\mathbf{F}_{ab}^I = \begin{cases} s_{ab} \frac{m_a + m_b}{2} \cos\left(\frac{1.5\pi}{kh} r_{ab}\right) \frac{\mathbf{r}_{ab}}{r_{ab}}, & r_{ab} \leq kh \\ 0, & r_{ab} > kh \end{cases}, \quad (13)$$

where  $s_{ab}$  is the strength of the force acting between particles  $a$  and  $b$ . In this paper, the value of  $s_{ab}$  is 5. It should be noted that the force  $\mathbf{F}_{ab}^I$  used here is the force used in Ref. [27] multiplied by a factor  $(m_a + m_b)/2$ . Therefore the last term in Eq. (12) does not vary with particle mass, and even if particles with different masses are used, the value of  $s_{ab}$  is the same for all particles.

The force  $\mathbf{F}^I$  is repulsive with particle spacing  $r_{ab} < kh/3$  and attractive when  $kh/3 < r_{ab} < kh$ . For uniformly distributed particles (i.e., particles in the interior domain), the interparticle forces from neighboring particles will be balanced. In contrast, for nonuniformly distributed particles such as the particles around free surfaces, particles at the free

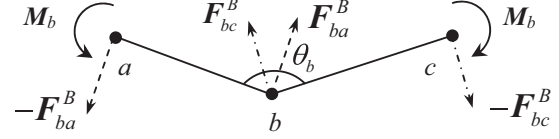


FIG. 4. An EBG is made of two adjacent line segments connecting three neighboring particles. In the EBG model, the bending moment is converted to pairs of forces acting on particles.

surface for example, the interparticle forces will no longer be balanced. Thus the interparticle force  $\mathbf{F}^I$  acts as a surface tension, which can be used to mimic the surface tension effect on the soap film in Alben *et al.*'s experiment [10]. It is also noted that  $\mathbf{F}^I$  can also help to remove a fake numerical phenomenon with empty (or void) area behind the fiber when it moves rapidly.

### C. EBG model for flexible fiber

In this paper, the movement and deformation of a flexible fiber is modeled by using the EBG model, which replaces the fiber with particles. Fiber particles can interact with neighboring fiber particles and fluid particles. In the EBG model, bending moment is transformed to pairs of forces acting on particles [23,25]. An EBG is made of two adjacent line segments connecting three neighboring particles (see Fig. 4).

According to Newton's second law of motion, the equation for a flexible fiber particle can be written as follows:

$$m \frac{d\mathbf{u}}{dt} = \mathbf{T} + \mathbf{F}^B + \mathbf{F}^D + \mathbf{g}, \quad (14)$$

where  $\mathbf{T}$  denotes the tension acting on a fiber particle from adjacent fiber particles,  $\mathbf{F}^B$  denotes the force due to EBG bending moment,  $\mathbf{F}^D$  denotes the fluid force from neighboring fluid (SPH) particles.

The tension can be calculated as

$$\mathbf{T}_{ba} = EA \left( \frac{r_{ab}}{r_{ab}^0} - 1 \right) \frac{\mathbf{r}_{ab}}{r_{ab}}, \quad (15)$$

where  $E$  and  $A$  are the Young's modulus and the cross-sectional area of the fiber, respectively, and  $r_{ab}^0$  is the reference distance between particles  $a$  and  $b$ . In order to reduce the length fluctuation down to 1%,  $EA$  is taken 2 orders of magnitude higher than the maximum tension along the fiber.

The force  $\mathbf{F}_{ba}^B$  acting on particle  $b$  from particle  $a$  due to EBG satisfies the following equation:

$$\mathbf{M}_b = \mathbf{r}_{ab} \times \mathbf{F}_{ba}^B \quad (16)$$

or

$$\mathbf{F}_{ba}^B = \frac{\mathbf{M}_b \times \mathbf{r}_{ab}}{r_{ab}^2}, \quad (17)$$

where  $\mathbf{M}_b$  denotes the moment acting on particle  $b$  (see Fig. 4), which is defined as

$$\mathbf{M}_b = \frac{EI(\theta_b - \theta_b^0)}{r_{ba} + r_{bc}}, \quad (18)$$

where  $EI$  and  $\theta$  is the bending rigidity and the deflection of the flexible fiber, respectively.  $\theta_b^0$  is the reference deflection



This kind of boundary condition was used in SPH by Yang and Liu [29] in modeling oil spill and boom movement, and it showed good performances in damping wave energy and vortices.

The flow in porous media in our simulations can be described by the following equation [30,31]:

$$\frac{d\mathbf{u}}{dt} = \mathbf{g} - \frac{1}{\rho} \nabla p + \nu \nabla^2 \mathbf{u} - \left( \frac{\nu n_w}{K_p} + \frac{C_f n_w^2}{\sqrt{K_p}} \mathbf{u} \right) \mathbf{u}_y, \quad (23)$$

where  $n_w$  is the porosity of the porous media,  $u$  is the magnitude of fluid velocity (e.g.,  $u = |\mathbf{u}|$ ),  $K_p$  is the intrinsic permeability, and  $C_f$  is the dimensionless turbulent resistance coefficient.  $K_p$  and  $C_f$  can be determined as follows [30,31]:

$$K_p = 1.643 \times 10^{-7} \frac{n_w^3}{(1 - n_w)^2} \left( \frac{d}{d_0} \right)^{1.57}, \quad (24)$$

$$C_f = 100 \left( d \sqrt{\frac{n_w}{K_p}} \right)^{-1.5}, \quad (25)$$

where  $d_0 = 0.01$  m. In all the following simulations in this paper we take  $d = 0.001$  m and  $n_w = 0.9$ , then from Eqs. (24) and (25) we have  $K_p = 3.2 \times 10^{-7}$  and  $C_f = 46.3$ .  $\mathbf{u}_y$  denotes that the damping term in Eq. (23) is used only in the  $y$  direction, that is, in the  $x$  direction the last term on the right-hand side of Eq. (23) is equal to zero. By using the layer of porous media, the wave energy and vortices can be effectively absorbed and the inlet flow can be adjusted uniformly.

### III. RESULTS AND DISCUSSIONS

In this section, the interaction of flexible fibers with viscous fluid is numerically investigated using the above-described SPH-EBG model. Simulations with three flexible fibers of length 3.3, 5.0, and 8.0 cm, and a rigid fiber of length 2.0 cm were run, respectively. The system is simulated with initial particle spacing of 0.1 cm, numerical sound speed 100 m/s, and time step  $1 \times 10^{-6}$  s. Here 36 000 particles are used to describe the fluid, and 34, 51, 81, and 21 particles are used to describe the fibers of length 3.3, 5.0, 8.0, and 2.0 cm, respectively.

#### A. Bending modes of flexible fibers

The shape of the fiber changes during the fluid-flexible fiber interaction process. Figure 6 shows three typical bending modes of flexible fibers, namely, the U-shaped mode, the flapping mode, and the closed mode. It is shown that as the flow velocity increases from zero, the fiber becomes more bent and more streamlined. Thus the flexible fiber is folded with a stable U shape [Fig. 6(a)]. For a U-shaped flexible fiber, the two ends of the fiber approach each other slowly and then swing slightly due to the appearance of vortex shedding. Gradually increasing the flow velocity before a critical value can produce a rich variety of fiber configurations because of vortex shedding. Around this critical velocity, the ends of the fiber will flap with large amplitude [Fig. 6(b)] which is similar to a flapping flag [32,33]. When further increasing the flow velocity, the two ends of the fiber may combine together and form a closed structure [Fig. 6(c)]. This is different from the

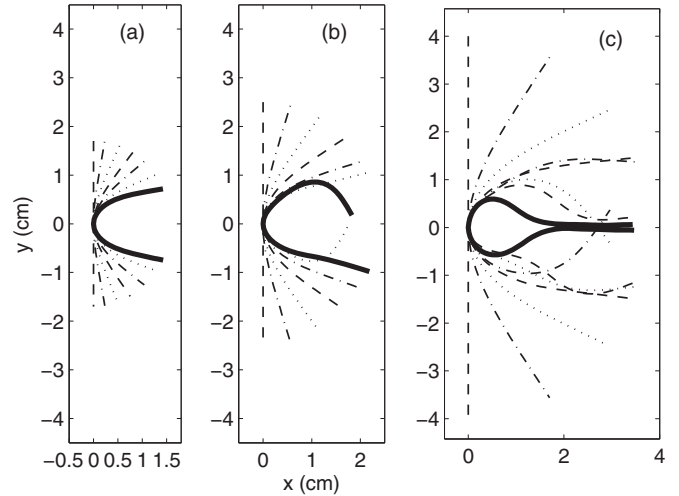


FIG. 6. Three typical bending modes of flexible fibers: (a) U-shaped mode ( $L = 3.3$  cm), (b) flapping mode ( $L = 5.0$  cm), and (c) closed mode ( $L = 8.0$  cm).

numerical solutions obtained by Alben *et al.* [11]. In their numerical solutions, the fiber bends and becomes progressively more aligned with the far field flow as the flow speed increases, and there is no fiber flapping and no closed fiber shapes.

Figure 7 shows the  $y$  coordinates of the endpoints of three flexible fibers of length  $L = 3.3$ , 5.0, and 8.0 cm, respectively. It is found that the flapping of flexible fibers is caused by vortex shedding. For the three flexible fibers of different lengths, vortex shedding all appeared at about 1.5 m/s flow velocity. However, the fiber does not flap immediately when vortex shedding appears. From Fig. 7 it can be seen that the fiber

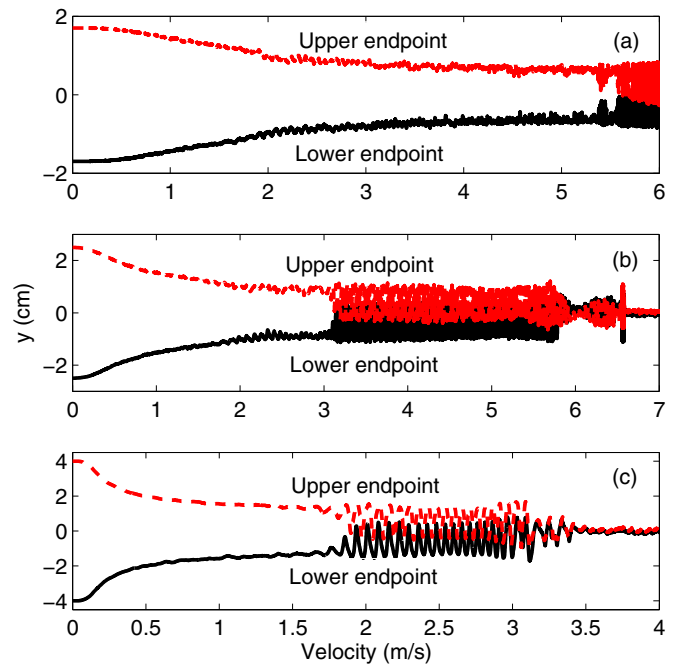


FIG. 7. (Color online) The  $y$  coordinates of the two endpoints vs velocity for flexible fibers with different lengths: (a)  $L = 3.3$  cm, (b)  $L = 5.0$  cm, and (c)  $L = 8.0$  cm.

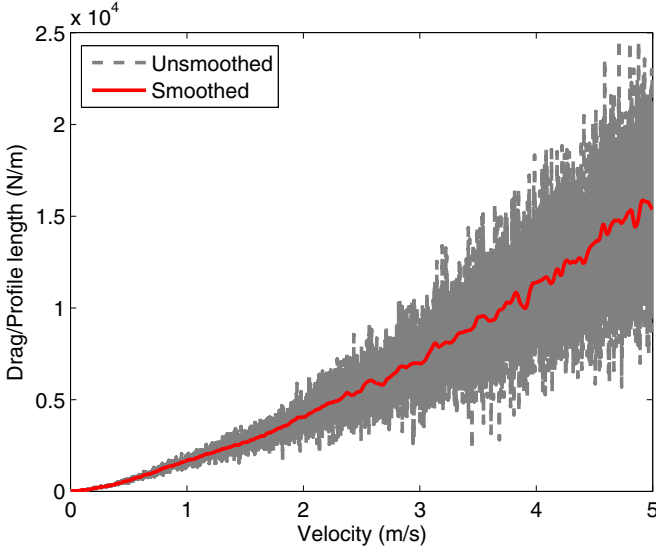


FIG. 8. (Color online) Comparisons of smoothed and unsmoothed drag for the flexible fiber of length  $L = 3.3$  cm.

began to flap at about 5.5, 3.1, and 1.8 m/s flow velocity for fibers of length 3.3, 5.0, and 8.0 cm. Thus a longer flexible fiber is easier to flap when the rigidity of the fiber stays unchanged.

### B. Drag scaling

In particle modeling of fluid-fiber interaction, vortices at different scales are frequently generated and shed, which leads to flow fluctuation and flexible fiber oscillation. As such, the obtained numerical results may also experience some oscillations. In order to obtain small fluctuations, the numerical data of fluid drag are smoothed as follows:

$$D_s = \frac{\sum_t D_t W_{st}^t}{\sum_t W_{st}^t}, \quad (26)$$

where  $D_s$  denotes the smoothed fluid drag at time  $s$ ;  $D_t$  denotes the unsmoothed fluid drag at time  $t$ ; and  $W^t$  is a smoothed kernel which has the same form as the kernel function shown in Eq. (5), but with variables of different means and values:

$$W^t(s') = \begin{cases} (2 - s')^3 - 4(1 - s')^3, & 0 \leq s' < 1 \\ (2 - s')^3, & 1 \leq s' < 2 \\ 0, & s' \geq 2 \end{cases}, \quad (27)$$

where  $s' = (s - t)/h^t$ , and  $h^t$  denotes a smoothed length of time that determines the time length of the smoothed kernel. Figure 8 compares the smoothed and unsmoothed drag for a flexible fiber of length  $L = 3.3$  cm. As shown in Fig. 8, the smoothed curve retains some tiny fluctuations, because the smoothed length of time  $h^t$  takes the value of 0.01 s. If  $h^t$  takes a larger value, the smoothed curve will be smoother. In the following contents, the drag and the coefficient of drag are all smoothed, while other data are not smoothed.

Figure 9 shows the fluid drag per unit profile length (which means the frontal length presented to the flow) versus flow velocity together with experimental observations from Alben *et al.* [10] for the rigid fiber of length  $L = 2.0$  cm and the flexible fiber of length  $L = 3.3$  cm. It is shown that the

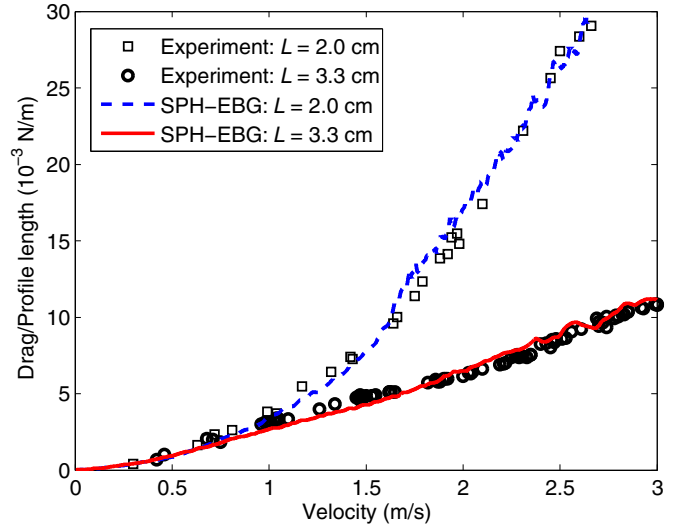


FIG. 9. (Color online) Numerical results compared with the experimental results from Alben *et al.* [10]. The fiber of length  $L = 2.0$  cm is a rigid fiber, and the corresponding converted thickness of the flow is  $2.1 \mu\text{m}$ . The fiber of length  $L = 3.3$  cm is a flexible fiber, and the corresponding converted thickness of the flow is  $1.6 \mu\text{m}$ . The thickness of soap film used in the experiment is in the range of  $1-3 \mu\text{m}$ .

numerical results agree very well with the experimental results for both the rigid and flexible fibers. It is demonstrated that the presented SPH-EBG coupling approach is effective in modeling both rigid and flexible fibers.

It should be noted that in order to compare with experimental data, the numerical data of drag in Fig. 9 obtained from SPH-EBG simulations are converted to the size of the experimental data as follows:

$$D^* = D \delta / \delta_0, \quad (28)$$

where  $\delta_0 = 1$  m denotes the thickness of 2D flow,  $\delta$  is the converted thickness,  $D^*$  is the converted drag, and  $D$  is the drag from 2D simulations. The thickness of the soap film in the experiment [10] is in the range of  $1-3 \mu\text{m}$ , but the thickness is not exactly known for each case. In fact, the thickness of the film is not exactly the same everywhere in the flow and it is also not a constant with respect to time [11,34]. The converted thickness is selected in the range of  $1-3 \mu\text{m}$  by comparing the converted drag with experimental drag. The converted thickness of the flow for the rigid fiber of length 2.0 cm is  $2.1 \mu\text{m}$ , and the converted thickness of the flow for the flexible fiber of length 3.3 cm is  $1.6 \mu\text{m}$ , respectively.

In order to study the drag scaling of fluid drag for fibers, the numerical drag is fitted using the function  $D = \alpha U^\beta$ , where  $\alpha$  is a coefficient and  $\beta$  denotes the exponent to which the drag must be raised to be proportional to flow velocity. For a rigid fiber of length  $L = 2.0$  cm (see Fig. 10), the fitted value of  $\beta$  is 2.10, which is very close to the theoretical value of 2. Figure 10 shows the variations of the drag with respect to fluid velocity for a rigid fiber of length  $L = 2.0$  cm. As shown in Fig. 10, there is a drag translation at flow velocity about 1.7 m/s. It is found that this drag transition happens when vortex shedding appears. If we fit the data in a piecewise manner, the exponent

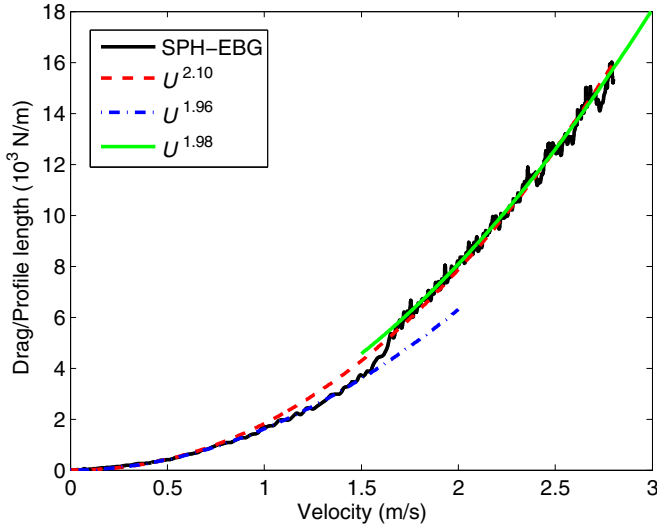


FIG. 10. (Color online) Fluid drag per unit profile length vs flow velocity for a rigid fiber of length  $L = 2.0$  cm. At a flow velocity of about 1.6 m/s, there is a drag transition because of vortex shedding.

values are different before and after vortex shedding. The value of  $\beta$  is 1.96 before and 1.98 after vortex shedding, respectively, closer than the total fitted value of 2.10 to the theoretical value of 2.

Figure 11 shows the log-log plots of fluid drag for the rigid and flexible fibers. It is shown in Fig. 11 that drag scaling is not valid when the flow velocity is smaller than about 0.2 m/s because of viscous force and numerical error. Although the drag acting on the rigid fiber changes obviously when vortex shedding appears (see Fig. 10), the drag scaling stays unchanged [see Fig. 11(a)]. It is also shown that the  $U^{4/3}$  drag scaling law for flexible fibers is only valid for a certain range of flow velocity [see Figs. 11(b)–11(d)]. When the flow velocity is bigger than about 3 m/s [see Figs. 11(c) and 11(d)],

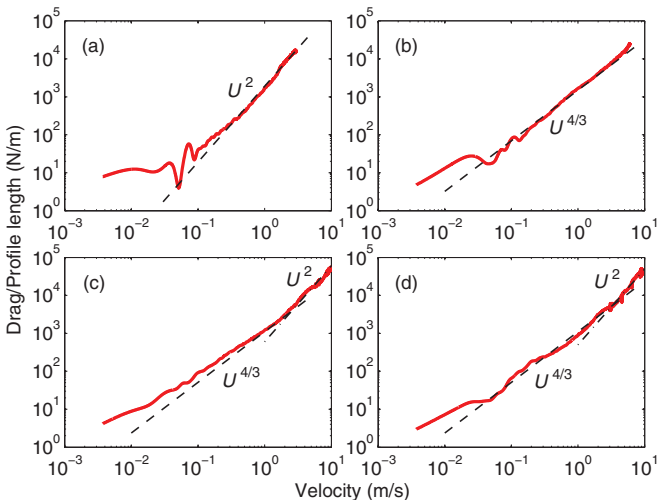


FIG. 11. (Color online) Log-log plots of fluid drag per unit profile length versus flow velocity for the rigid fiber of length  $L = 2.0$  cm (a) and the flexible fibers of length  $L = 3.3$  cm (b),  $L = 5.0$  cm (c), and  $L = 8.0$  cm (d).

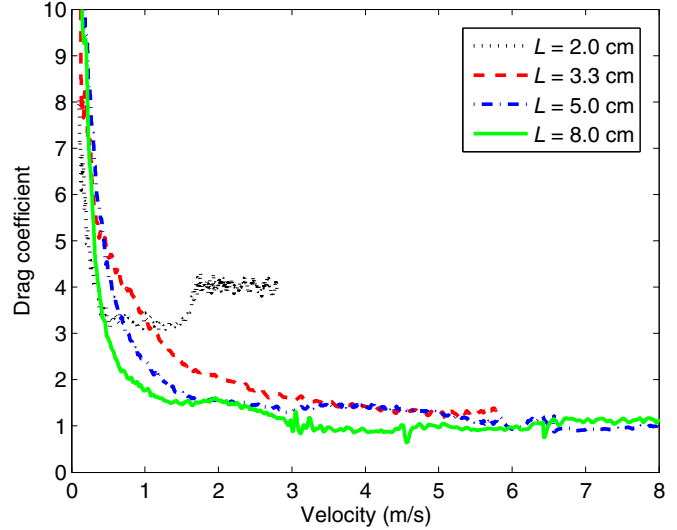


FIG. 12. (Color online) Drag coefficient versus flow velocity for the rigid fiber of length  $L = 2.0$  cm and three flexible fibers of length  $L = 3.3, 5.0,$  and  $8.0$  cm.

fluid drag acting on a flexible fiber is proportional to  $U^2$ , which is the same as the drag scaling of a rigid fiber. This is because the flexible fiber forms a closed shape (i.e., the closed mode as mentioned in previous section) and it is not able to become more streamlined through bending.

Figure 12 shows the drag coefficient versus flow velocity for the rigid and flexible fibers. The drag coefficient is defined as  $C_D = F^D / (\rho L_y u^2 / 2)$ , where  $F^D$  is drag force,  $\rho$  is fluid density,  $L_y$  is the profile length of a fiber in flow direction, and  $u$  is flow velocity.

For comparison, the drag coefficient of the rigid fiber with length 2.0 cm is also given in Fig. 12. It can be seen that the drag coefficient of the rigid fiber is bigger after the drag translation at flow velocity of about 1.7 m/s due to vortex shedding. The influence of vortex shedding on the drag coefficient of flexible fibers is not as much as that of the rigid fiber. One possible reason is that flexible fibers can flap with vortex shedding while rigid fibers cannot.

It is shown in Fig. 12 that the drag coefficients of flexible fibers reduce as the velocity increases, because flexible fibers become more streamlined as the fluid velocity increases, which is one of the main reasons for the drag reduction of flexible fibers. It can also be seen that the drag coefficient of a longer flexible fiber reduces more rapidly than that of a shorter one, because a longer fiber is easier to bend than a shorter one and a longer fiber forms a more streamlined shape. The drag coefficient of a flexible fiber is nearly a constant after the fiber forms a closed shape, e.g., after velocity of about 6.6 m/s for the fiber of length 5.0 cm and about 3.5 m/s for the fiber of length 8.0 cm.

### C. The influence of vortex

In the classical SPH method, particles are treated as points and a particle can only move from one point to another but cannot rotate. In order to visualize the vortices behind a fiber, the freedom of rotation of a SPH particle is released, which

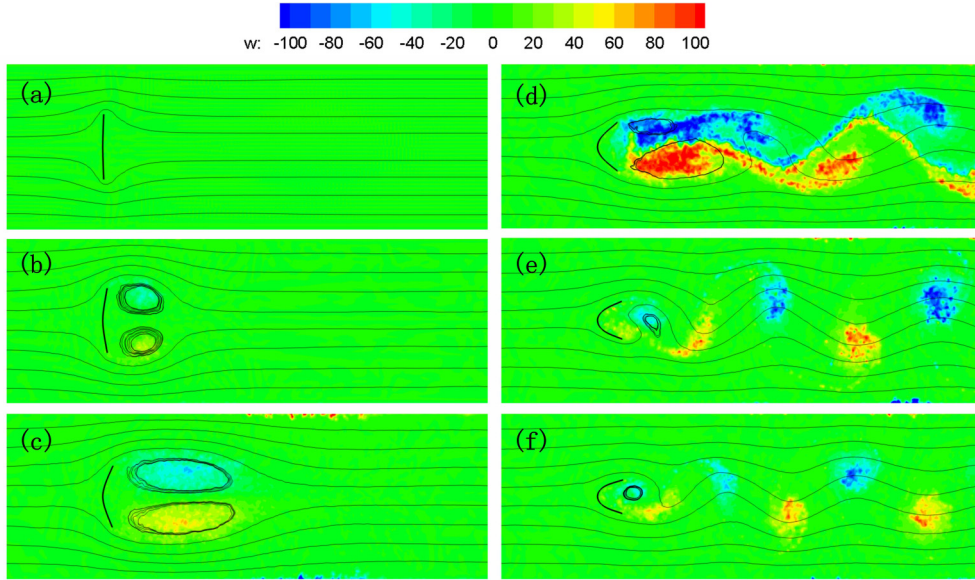


FIG. 13. (Color online) The streamlines and vortices of the flexible fiber of length  $L = 3.3$  cm at different times (and velocities): (a)  $t = 0.1$  s ( $u = 0.091$  m/s), (b)  $t = 0.3$  s ( $u = 0.335$  m/s), (c)  $t = 0.5$  s ( $u = 0.616$  m/s), (d)  $t = 1.0$  s ( $u = 1.403$  m/s), (e)  $t = 1.3$  s ( $u = 1.988$  m/s), and (f)  $t = 1.5$  s ( $u = 2.428$  m/s). The lines are streamlines and the color shows the angular velocity of SPH particles.

means that an SPH particle can rotate if there is a moment of force acting on it. The force moment on a particle due to viscosity is defined as follows:

$$\mathbf{M}_a^v = l^v \sum_b \frac{\mathbf{r}_b - \mathbf{r}_a}{r_{ab}} \mathbf{F}_{ab}^v W_{ab} \frac{m_b}{\rho_b}, \quad (29)$$

where  $\mathbf{F}_{ab}^v$  is the viscous force acting on particle  $a$  due to particle  $b$ , and  $l^v$  is viscous length, which defines the influence domain of viscosity. The value of  $l^v$  is in the order of the initial particle spacing. The corresponding angular acceleration of

particle  $a$  is defined as

$$\frac{d\omega_a}{dt} = \frac{\mathbf{M}_a^v}{I_a}, \quad (30)$$

where  $\omega_a$  and  $I_a$  denote the angular velocity and the momentum of inertia of particle  $a$ , respectively. Then the angular velocity of a particle can be obtained by integrating Eq. (30).

It should be noted that in this paper the angular velocities of particles are only used to show the vortex structures of the flow, because the rotations of fluid particles are related to the fluid

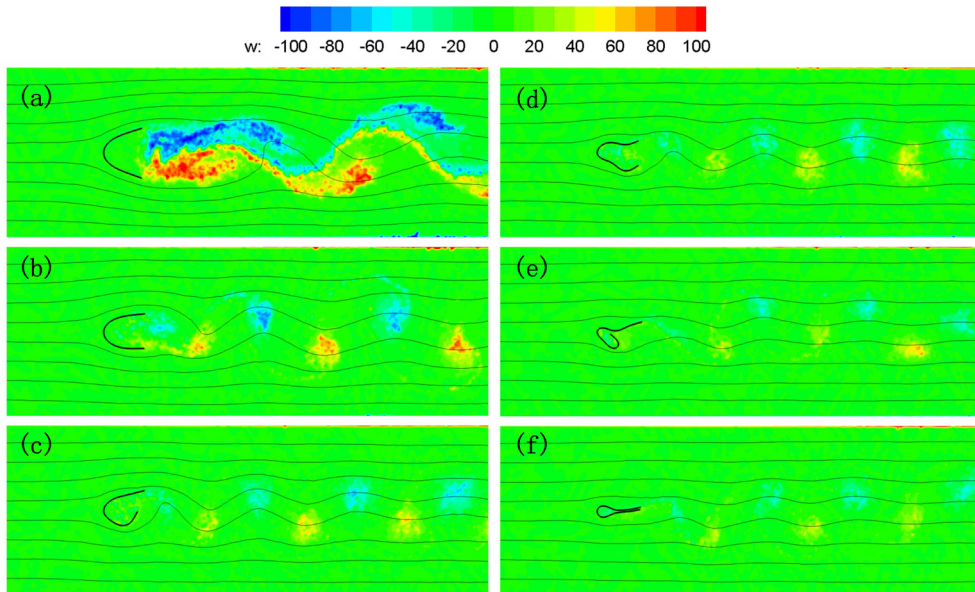


FIG. 14. (Color online) The streamlines and vortices of the flexible fiber of length  $L = 5.0$  cm at different times (and velocities): (a)  $t = 1.0$  s ( $u = 1.497$  m/s), (b)  $t = 1.5$  s ( $u = 2.671$  m/s), (c)  $t = 2.0$  s ( $u = 3.644$  m/s), (d)  $t = 3.0$  s ( $u = 5.103$  m/s), (e)  $t = 3.8$  s ( $u = 6.573$  m/s), and (f)  $t = 3.85$  s ( $u = 6.586$  m/s). The lines are streamlines and the color shows the angular velocity of SPH particles.

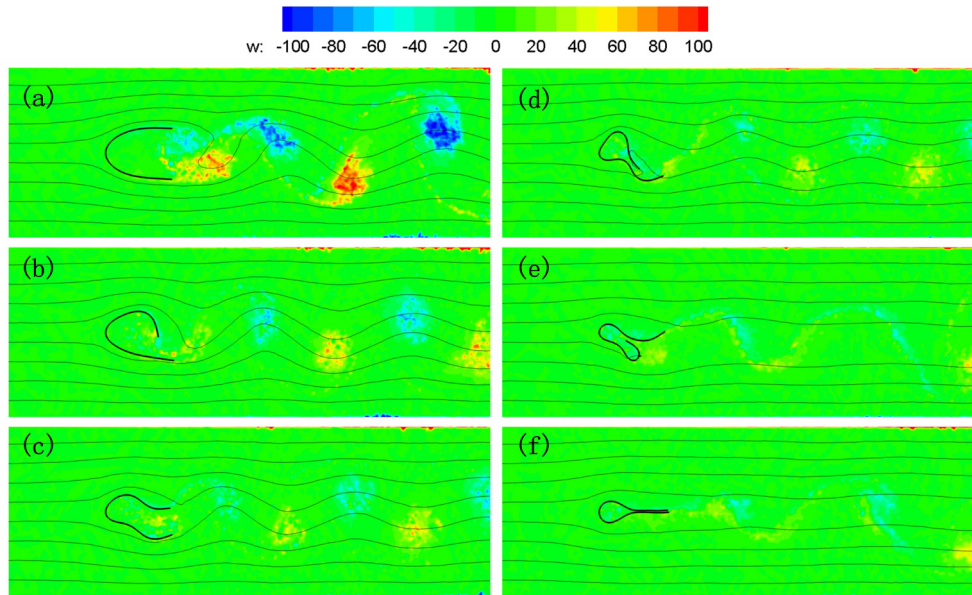


FIG. 15. (Color online) The streamlines and vortices of the flexible fiber of length  $L = 8.0$  cm at different times (and velocities): (a)  $t = 1.0$  s ( $u = 1.609$  m/s), (b)  $t = 1.3$  s ( $u = 2.198$  m/s), (c)  $t = 1.6$  s ( $u = 2.780$  m/s), (d)  $t = 1.7$  s ( $u = 2.992$  m/s), (e)  $t = 1.8$  s ( $u = 3.271$  m/s), and (f)  $t = 1.85$  s ( $u = 3.455$  m/s). The lines are streamlines and the color shows the angular velocity of SPH particles.

vortices [35,36]. Although the angular velocity of a particle is determined by the flow, it does not affect the flow, and the rotations of the particles do not interact with each other.

Figures 13–15 show streamlines and vortices at different times (and velocities) for three flexible fibers of length  $L = 3.3, 5.0,$  and  $8.0$  cm, respectively. It is obvious that during the flexible fiber–fluid interaction process, the shape of the fiber changes because the fiber bends more and more and forms a streamlined shape. As shown in Figs. 13–15, the downstream flows are associated with vortices and curved streamlines, while the upstream flows (especially at the entrance) are even with straight lines. This clearly shows the effectiveness of the inflow boundary treatment with a layer of porous media in removing the influence on inlet flows from the downstream flows when applying the periodic boundary used in the flow direction.

In the initial stage, at low velocities two symmetric vortices generate at the two ends of the fiber [Figs. 13(a)–13(c)]. As the flow velocity increases, the width and length of the vortices increase, especially the length in the flow direction. However, at a certain velocity, the two symmetric vortices translate to two rows of asymmetric vortices [Fig. 13(d)], which is the so-called Kármán vortex street [37]. The vortex street will finally reach a stable state as the flow field is well developed [Figs. 13(e) and 13(f)].

Comparing the flexible fibers of length  $L = 3.3, 5.0,$  and  $8.0$  cm with each other, it is found that the bending form of a longer fiber is more complicated. As the vortex shedding becomes stronger, the flexible fiber can no longer remain in U shape and starts to flap at a certain flow velocity. Before a closed structure forms, the flexible fiber will flap violently. The bending angle is greater than 90 degrees and sometimes approaches even 180 degrees [see Figs. 14(e) and 15(e)]. It is obvious that the flapping of a flexible fiber is caused by vortex shedding. It can be expected that the flexible

fiber will remain in U-shaped mode as the flow velocity increases if there is no vortex shedding.

It is an interesting work to study the influence of vortex shedding on the drag of a flexible fiber. Zhu [15] numerically studied the influence of three dimensionless parameters on the structure of shed vortices for Reynolds numbers in the range of 30–800. Vortex shedding and vortex-introduced vibration of flexible fibers were investigated in detail in Refs. [15,38] regarding other aspects.

#### IV. CONCLUSIONS

In this paper, a numerical approach is presented for modeling the interaction of viscous fluids and flexible fibers. The numerical approach is based on the coupling of the SPH method and the EBG technique. As both SPH and EBG are Lagrangian particle methods, the SPH-EBG coupling approach is also a Lagrangian particle approach that is suitable for modeling physics with moving and deformable features. In the SPH-EBG approach, SPH particles are used to represent the fluid, EBG particles are used to represent the flexible fiber, and the fiber-fluid interaction is implemented through allowing the interaction of neighboring SPH and EBG particles. The SPH-EBG approach is applied to model the interaction of a viscous fluid with rigid and flexible fibers of different lengths.

From the SPH-EBG simulations, three bending modes of flexible fibers are observed, namely, the U-shaped mode, the flapping mode, and the closed mode. For the U-shaped mode, the flexible fiber becomes more streamlined as the flow velocity increases. For the flapping mode, the flexible fiber flaps with large amplitude due to strong vortex shedding. For the closed mode, the two ends of the flexible fiber combine with each other.

The numerical results show that fluid drags scaling on both rigid and flexible fibers agree well with those from

experimental observations [10], dimensional analysis [12], and other numerical modeling [39]. However, the  $U^{4/3}$  drag scaling law for a flexible fiber is valid only for the U-shaped mode but not for the flapping and closed modes. The drag scaling for a flexible fiber in closed mode is the same as that for a rigid body, e.g., the drag is proportional to the square of velocity. The drag scaling for a flexible fiber in flapping mode seems different for different fibers.

It is also shown that vortex shedding is of significant importance for the interaction of fluid and fibers. It led to a transition

of the fluid drag of the rigid fiber. It is also vortex shedding, which causes different bending modes of flexible fibers.

#### ACKNOWLEDGMENT

We thank Professor S. Alben for providing us with the experimental data in Fig. 9. This work was supported by the National Natural Science Foundation of China (Grants No. 11302237 and No. 11172306).

- 
- [1] B. R. Munson, D. F. Young, T. H. Okiishi, and W. W. Huebsch, *Fundamentals of Fluid Mechanics*, 6th ed. (Wiley, New York, 2009).
  - [2] S. Vogel, *Life in Moving Fluids: The Physical Biology of Flow* (Princeton University Press, Princeton, NJ, 1994).
  - [3] M. J. Shelley and J. Zhang, *Annu. Rev. Fluid Mech.* **43**, 449 (2011).
  - [4] F. P. Gosselin and E. De Langre, *J. Fluids Struct.* **27**, 1111 (2011).
  - [5] I. Albayrak, V. Nikora, O. Miler, and M. T. O'Hare, *Aquat. Sci.* **76**, 269 (2014).
  - [6] S. Vogel, *J. Exp. Bot.* **40**, 941 (1989).
  - [7] E. de Langre, A. Gutierrez, and J. Cossé, *C. R. Mec.* **340**, 35 (2012).
  - [8] H.-C. Spatz and B. Theckes, *Plant Science* **207**, 66 (2013).
  - [9] P. Whittaker, C. Wilson, J. Aberle, H. P. Rauch, and P. Xavier, *J. Hydraulic Research* **51**, 569 (2013).
  - [10] S. Alben, M. Shelley, and J. Zhang, *Nature (London)* **420**, 479 (2002).
  - [11] S. Alben, M. Shelley, and J. Zhang, *Phys. Fluids* **16**, 1694 (2004).
  - [12] F. Gosselin, E. de Langre, and B. A. Machado-Almeida, *J. Fluid Mech.* **650**, 319 (2010).
  - [13] M. Luhar and H. M. Nepf, *Limnol. Oceanogr.* **56**, 2003 (2011).
  - [14] L. Zhu and C. S. Peskin, *Computers & Fluids* **36**, 398 (2007).
  - [15] L. Zhu, *J. Fluid Mech.* **587**, 217 (2007).
  - [16] L. B. Lucy, *Astron. J.* **82**, 1013 (1977).
  - [17] R. A. Gingold and J. J. Monaghan, *Mon. Not. R. Astron. Soc.* **181**, 375 (1977).
  - [18] J. J. Monaghan, *Annu. Rev. Fluid Mech.* **44**, 323 (2012).
  - [19] J. P. Morris, P. J. Fox, and Y. Zhu, *J. Comput. Phys.* **136**, 214 (1997).
  - [20] S. Shao and E. Y. M. Lo, *Adv. Water Res.* **26**, 787 (2003).
  - [21] G. R. Liu and M. B. Liu, *Smoothed Particle Hydrodynamics: A Meshfree Particle Method* (World Scientific, Singapore, 2003).
  - [22] M. B. Liu, G. R. Liu, and K. Y. Lam, *J. Comput. Appl. Math.* **155**, 263 (2003).
  - [23] D. Zhou and R. Wagoner, *J. Mater. Process. Technol.* **50**, 1 (1995).
  - [24] K.-i. Tsubota, S. Wada, and T. Yamaguchi, *Journal of Biomechanical Science and Engineering* **1**, 159 (2006).
  - [25] S. M. Hosseini and J. J. Feng, *Chem. Eng. Sci.* **64**, 4488 (2009).
  - [26] J. J. Monaghan, *Rep. Prog. Phys.* **68**, 1703 (2005).
  - [27] A. Tartakovsky and P. Meakin, *Phys. Rev. E* **72**, 026301 (2005).
  - [28] R. W. Hockney and J. W. Eastwood, *Computer Simulation Using Particles* (Taylor & Francis, Boca Raton, FL, 1988).
  - [29] X. F. Yang and M. B. Liu, *Sci. China-Phys. Mech. Astron.* **56**, 315 (2013).
  - [30] C. K. Sollitt and R. H. Cross, in *Proceedings of the 13th International Conference on Coastal Engineering* (American Society of Civil Engineers, 1972), pp. 1827–1846.
  - [31] C.-J. Huang, H.-H. Chang, and H.-H. Hwung, *Coastal Eng.* **49**, 1 (2003).
  - [32] S. Michelin, S. G. Llewellyn Smith, and B. J. Glover, *J. Fluid Mech.* **617**, 1 (2008).
  - [33] L. Zhu and C. S. Peskin, *Phys. Fluids* **15**, 1954 (2003).
  - [34] V. Steinberg, *Nature (London)* **420**, 473 (2002).
  - [35] Z. Zhang and G. Cui, *Fluid Mechanics* (Tsinghua University Press, Beijing, 2006) (in Chinese).
  - [36] J.-Z. Wu, H.-Y. Ma, and M.-D. Zhou, *Vorticity and Vortex Dynamics* (Springer-Verlag, Berlin, 2006).
  - [37] H. Oertel, P. Erhard, K. Asfaw, D. Etling, U. Muller, U. Riedel, K. Sreenivasan, and J. Warnatz, *Prandtl—Essentials of Fluid Mechanics* (Springer, Berlin, 2010).
  - [38] L. A. Miller, A. Santhanakrishnan, S. Jones, C. Hamlet, K. Mertens, and L. Zhu, *J. Exp. Biol.* **215**, 2716 (2012).
  - [39] L. Zhu, *J. Fluid Mech.* **607**, 387 (2008).